Radiative and nonradiative charge transfer in collisions of Be^{2+} and B^{3+} ions with H atoms

C. H. Liu,[1] L. Liu,[1,2] Y. Z. Qu,[2] J. G. Wang,[1] and R. K. Janev[3,4]

[1]*Key Laboratory of Computational Physics, Institute of Applied Physics and Computational Mathematics, P.O. Box 8009, Beijing 100088, People's Republic of China*

[2]*College of Material Sciences and Optoelectronic Technology, Graduate University of the Chinese Academy of Sciences, P.O. Box 4588, Beijing 100049, People's Republic of China*

[3]*Macedonian Academy of Sciences and Arts, P.O. Box 428, 1000 Skopje, Macedonia*

[4]*Institut für Energieforschung–Plasmaphysik, Forschungszentrum Jülich GmbH, EURATOM Association, Trilateral Euregio Cluster, D-52425 Jülich, Germany*

(Received 9 May 2010; published 17 August 2010)

The nonradiative charge-transfer processes in $Be^{2+}(1s^2) + H(1s)$ and $B^{3+}(1s^2) + H(1s)$ collisions are investigated by the quantal molecular orbital close-coupling method in the energy range of 10^{-5}eV/u–10 keV/u and by the two-center atomic-orbital close-coupling method in the energy range of 0.1–100 keV/u. The radiative charge-transfer cross sections are calculated by using the optical potential and semiclassical methods in the energy range 10^{-5}–100 eV/u. For both collision systems, the nonradiative charge-transfer cross sections in the low-energy region show an increasing behavior with decreasing energy. The nonradiative process is the dominant charge-transfer process in the $Be^{2+}(1s^2) + H(1s)$ collision in the entire eV and sub-eV energy region. In the $B^{3+}(1s^2) + H(1s)$ collision case, however, the cross section for radiative decay to $1\,^2\Sigma^+$ and $2\,^2\Sigma^+$ molecular states significantly exceeds that for the nonradiative process for energies below 30 eV/u.

DOI: 10.1103/PhysRevA.82.022710 PACS number(s): 34.70.+e, 34.20.−b

I. INTRODUCTION

Beryllium and boron are important impurity species in the edge plasmas of thermonuclear fusion devices. Boron is released in the plasma from boronized graphites used as plasma facing materials in many tokamaks because of the plasma-wall interaction processes, while beryllium is envisaged as a first wall material in the International Thermonuclear Experimental Reactor [1]. The cross sections of various inelastic processes of these impurities in all charge states with the hydrogen plasma constituents are required for modeling of their transport in the plasma and their contribution to the plasma energy and particle losses. The charge-exchange processes of low-charged ions of these species with the neutral atomic hydrogen, both present in the relatively cold plasma edge regions, play an important role in the charge-state balance and neutral hydrogen losses. As the electron capture in these collisions populates mainly the excited states of reaction products, these processes also contribute to the edge plasma cooling.

The charge-transfer processes of He-like Be^{2+} and B^{3+} ions with H atoms have so far been theoretically studied in the energy region above 100 eV/u [2–9]. The only experimental study of these systems is that for $B^{3+} + H$ of Crandall *et al.* [10] in the energy range 1–10 keV/u. We should mention that the typical tokamak edge plasma temperatures are in the range 0.1–500 eV [1], and cross sections for charge-exchange processes in the previously mentioned collision systems are required in the energy region below 100 eV/u as well.

In this article, we shall study the charge-transfer processes in the Be^{2+} and B^{3+} collisions with atomic hydrogen using the quantal molecular orbital close-coupling (QMOCC) method in the energy range 10^{-5} eV/u–10 keV/u and the two-center atomic-orbital close-coupling (TC-AOCC) method in the energy range 0.1–100 keV/u. We note that the TC-AOCC method has been used for study of these reactions in the same energy range but employing a smaller expansion basis [9]. We shall also study the radiative charge-transfer process by the optical potential method in the 10^{-5}–0.1 eV/u energy range and by the semiclassical method in the 0.1–100 eV/u energy range. The cross sections of radiative charge-transfer processes are generally much smaller than those of nonradiative ones, but in certain collision systems (e.g., in $B^{3+} + H$), they may exceed those of nonradiative charge transfer at energies below ∼1–10 eV/u. In such cases, they may have significant importance in astrophysics [11].

The molecular structure data (potential curves, radial and rotational couplings, and dipole transition matrix elements) required in the QMOCC and radiative charge-transfer calculations have been calculated using the multireference single- and double-excitation configuration interaction (MRD-CI) method [12,13] that employs Gaussian-type orbitals.

II. MOLECULAR STRUCTURE CALCULATIONS

A. BeH^{2+} molecular ion

The *ab initio* CI calculation has been carried out for the potential energy curves of the lower six $^2\Sigma$ electronic states and three $^2\Pi$ states of the BeH^{2+} molecule by using the MRD-CI package [12,13]. In the calculations of hydrogen, the correlation-consistent, polarization valence, quadruple-z-(cc-pVQZ)-type basis set [14] with a diffuse $(2s3p)$ set was used. The cc-pVTZ-type basis set [14] with a diffuse $(2s2p2d1f)$ basis was employed for Be atoms. The final contracted basis set for the hydrogen atom was $(8s,6p,2d,1f)/[6s,6p,2d,1f]$ and that for the beryllium atom was $(13s,7p,4d,2f)/[6s,5p,4d,2f]$. A threshold of 10^{-8} hartree was used to select the configurations for BeH^{2+} at the internuclear distances between 0.5 and 30 a.u. As shown in Table I, the errors in the calculated energies with respect to the experimental atomic energies [15] are less than 0.07 eV in the asymptotic region. This accuracy level is quite adequate

TABLE I. Asymptotic separated-atom energies of BeH^{2+}.

Molecular state	Asymptotic atomic states	Energy (eV)		
		Theory	Experiment [15]	Difference
$1\,^2\Sigma$	$Be^+(2s)+H^+$	0	0	0
$2\,^2\Sigma$	$Be^{2+}+H(1s)$	4.550	4.613	0.063
$3\,^2\Sigma$	$Be^+(2p\sigma)+H^+$	3.968	3.959	0.009
$1\,^2\Pi$	$Be^+(2p\pi)+H^+$	3.968	3.959	0.009
$4\,^2\Sigma$	$Be^+(3s)+H^+$	10.943	10.940	0.003
$5\,^2\Sigma$	$Be^+(3p\sigma)+H^+$	11.949	11.964	0.015
$2\,^2\Pi$	$Be^+(3p\pi)+H^+$	11.949	11.964	0.015
$6\,^2\Sigma$	$Be^+(3d\sigma)+H^+$	12.154	12.158	0.004
$3\,^2\Pi$	$Be^+(3d\pi)+H^+$	12.154	12.158	0.004

for the present scattering calculations [16]. The obtained electronic wave functions are then used to calculate the radial and rotational couplings by employing finite differentiation and analytical approaches, respectively (see [17]).

In the present QMOCC calculations, allowance for the translation effects was made by introducing appropriate reaction coordinates [18,19], in which the radial and rotational coupling matrix elements between the states ψ_K and ψ_L are transformed into [20]

$$\langle\psi_K|\partial/\partial R-(\varepsilon_K-\varepsilon_L)z^2/2R|\psi_L\rangle,$$
$$\langle\psi_K|iL_y+(\varepsilon_K-\varepsilon_L)zx|\psi_L\rangle, \quad (1)$$

respectively, where ε_K and ε_L are the electronic energies of states ψ_K and ψ_L and z^2 and zx are the components of the quadrupole moment tensor. The modification is similar in form to that resulting from the application of the common electron translation factor (ETF) method [21].

The calculated adiabatic potentials for the considered molecular states of BeH^+ are shown in Fig. 1 for the internuclear distance $R = 0.5$–20 a.u. The $2\,^2\Sigma$ state represents the initial channel for this collision system. Figure 2 displays the radial coupling matrix elements for the BeH^{2+} ion with the ETF effects included. It is evident that the positions of the peaks in radial couplings are consistent with the avoided crossings of the adiabatic potentials observed in Fig. 1. It can be seen that the initial $2\,^2\Sigma$ state is strongly coupled with the $1\,^2\Sigma$ state at internuclear distances R about 6.7 a.u.; this is the main gateway of charge-transfer flux from the $2\,^2\Sigma$ state toward the exit channels. This coupling drives directly the transition to the $Be^+(2s)+H^+$ exit channel (see Table I). The coupling between the $2\,^2\Sigma$ and $3\,^2\Sigma$ states has its maximum at internuclear separations R about 3 a.u. and is much weaker than the $2\,^2\Sigma$–$1\,^2\Sigma$ coupling. The $2\,^2\Sigma$–$3\,^2\Sigma$ will play a significant role in the collision dynamics [particularly for the population of $Be^+(2p_0)+H^+$ exit channels] only at high collision energies when the small internuclear distances can be reached. Since in the region around $R \approx 3$ a.u. in Fig. 1 no avoided crossing is observed but rather a slight divergence of $2\,^2\Sigma$ and $3\,^2\Sigma$ potential curves from each other with increasing R, it is likely that the coupling of these states at $R \approx 3$ a.u. is of Demkov type. On the other hand, a clear and narrow avoided crossing between $2\,^2\Sigma$ and $3\,^2\Sigma$ potentials is observed at R about 46.7 a.u. (see the inset in Fig. 1), accompanied with a very sharp and narrow coupling matrix element of these states. Appearing at very large internuclear distances, this coupling does not induce noticeable transitions between the states, and it is passed by the system diabatically. However, it obviously is the first term in the series of avoided crossings $2\,^2\Sigma$–$3\,^2\Sigma$–$4\,^2\Sigma$–$5\,^2\Sigma$–$6\,^2\Sigma$, the higher terms of which are clearly observed either in Fig. 1 or in Fig. 2 through the sharp peaks in the corresponding matrix elements. We note that the $4\,^2\Sigma$–$5\,^2\Sigma$ and $5\,^2\Sigma$–$6\,^2\Sigma$ couplings with broad peaks at R around 5.5 a.u. and 5.0 a.u., respectively, are of Demkov type.

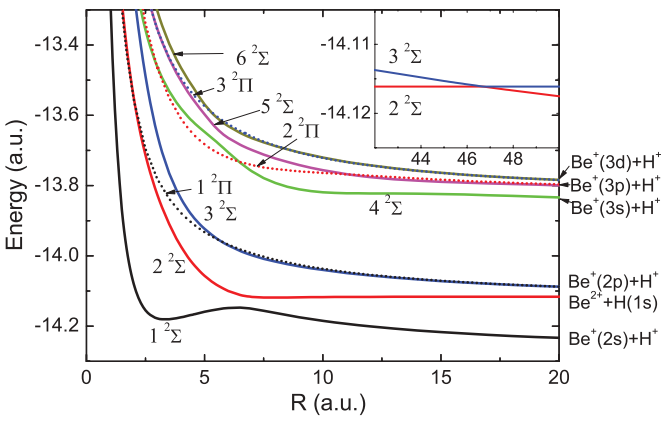

FIG. 1. (Color online) Adiabatic potential energy curves of BeH^{2+}. The solid and dotted lines represent the $^2\Sigma$ and $^2\Pi$ states, respectively. The inset shows the avoided crossing between $2\,^2\Sigma$ and $3\,^2\Sigma$ states at the internuclear distance about 46.7 a.u.

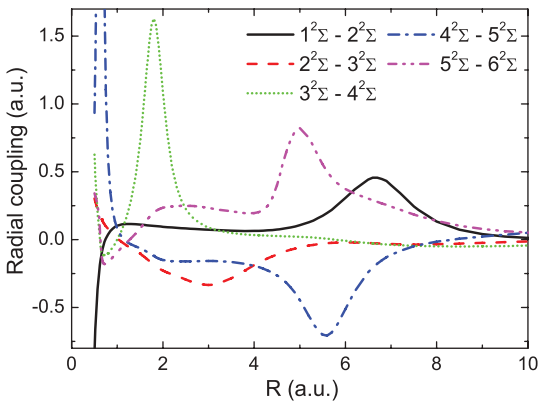

FIG. 2. (Color online) Radial coupling matrix elements between Σ states of BeH^{2+}.

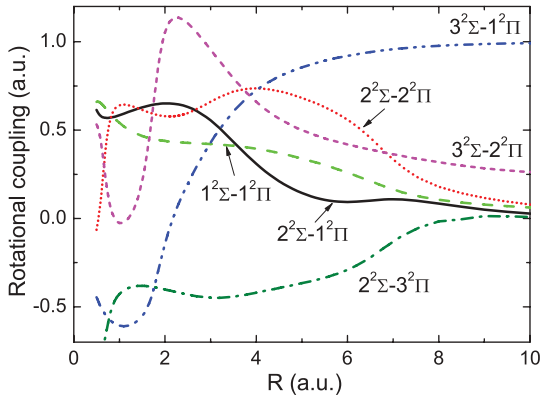

FIG. 3. (Color online) Rotational coupling matrix elements for BeH^{2+}.

As the $2\,^2\Sigma$–$3\,^2\Sigma$ coupling is weak (see Fig. 2), the population of $4\,^2\Sigma$, $5\,^2\Sigma$, and $6\,^2\Sigma$ molecular states through this series of couplings will also be small at low collision energies (and thereby the $n = 3$ charge-exchange channels).

Figure 3 shows some of the important rotational coupling matrix elements. The strongest among them in the region of R below 4–5 a.u. are the $2\,^2\Sigma$–$1\,^2\Pi$, $3\,^2\Sigma$–$1\,^2\Pi$, $2\,^2\Sigma$–$2\,^2\Pi$, and $3\,^2\Sigma$–$2\,^2\Pi$ couplings, the first two being responsible for the population of $Be^+(2p_1) + H^+$ exit channels, while the last two are responsible for the population of the $Be^+(3p_1) + H^+$ exit channel.

Figure 4 displays the dipole transition moment between $1\,^2\Sigma$ and $2\,^2\Sigma$ states, which is responsible for the radiative charge-transfer process in this collision system. The $1\,^2\Sigma$–$2\,^2\Sigma$ dipole transition moment is distributed in the range of internuclear distances between ∼1 a.u. and 10 a.u. with a sharp maximum around 6.7 a.u., the position of the avoided crossing between considered two states.

B. BH^{3+} molecular ion

We have performed electronic structure calculation for the lower six $^2\Sigma$ electronic states and three $^2\Pi$ states of the BH^{3+} ion by using the MRD-CI method. The cc-pVQZ-type basis set [14] was employed for the B atom, but the g-type basis was

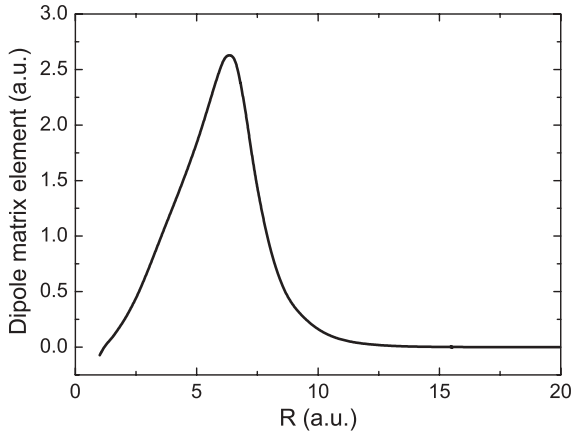

FIG. 4. Dipole transition matrix element between $1\,^2\Sigma$ and $2\,^2\Sigma$ states of BeH^{2+}.

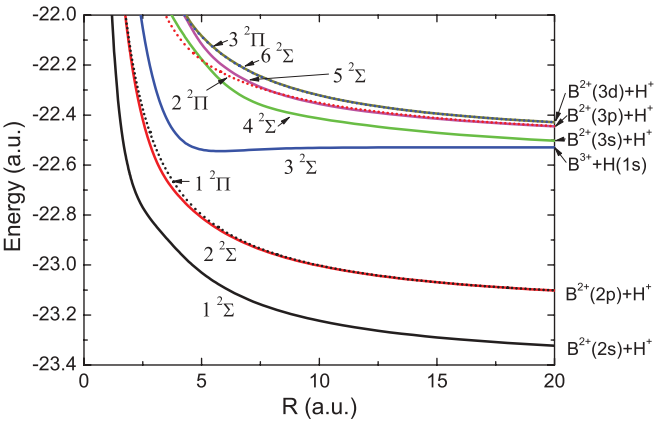

FIG. 5. (Color online) Adiabatic potential curves for BH^{3+}. The solid and dotted lines represent the $^2\Sigma$ and $^2\Pi$ states, respectively.

discarded. To the preceding basis set, the $(5s4p3d2f)$ diffuse functions were added. The final contracted basis set for the B atom was $(17s,10p,6d,4f)/[10s,8p,6d,4f]$. For the H atom, we have used the cc-pVQZ-type basis set. Table II compares the asymptotic energies in the separated-atom limit with the experimental atomic energies [15]. The error in the calculated energies is less than 0.015 eV in the asymptotic region.

The $3\,^2\Sigma$ state represents the initial channel of the $B^{3+} + H$ collision system. Figure 5 shows the calculated adiabatic potentials for internuclear distances $R = 0.5$–20 a.u. Figures 6 and 7 display the most important radial and rotational couplings between the considered states of BH^{3+}, respectively. Unlike the $Be^{2+} + H(1s)$ case, there are no effective avoided crossings between the initial $3\,^2\Sigma$ state with other molecular states of the $B^{3+} + H$ system for internuclear distances larger than 2 a.u. (see Fig. 6) to induce strong nonadiabatic couplings at low collision energies. Table II and Fig. 5 indicate that the initial $3\,^2\Sigma$ state energetically lies very close to the $B^{2+}(n = 3) + H^+$ states at large internuclear distances, but Fig. 6 shows that there is no strong radial coupling of $3\,^2\Sigma$ with the $4\,^2\Sigma^+$, $5\,^2\Sigma^+$, and $6\,^2\Sigma$ states at these distances. This signifies that the change of atomic character of asymptotic states into a molecular one takes place in an adiabatic manner when the internuclear distance decreases so that no nonadiabatic mixing effects (e.g., Demkov-type coupling) can appear between them.

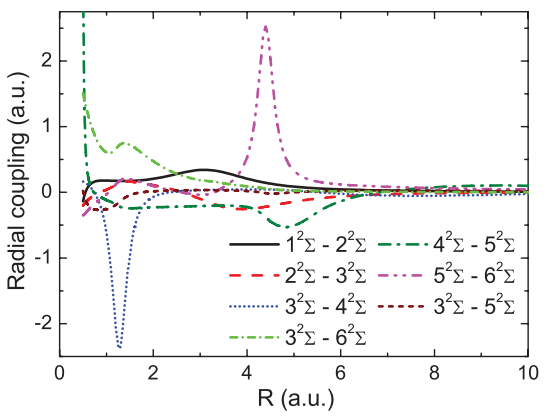

FIG. 6. (Color online) Radial coupling matrix elements for BH^{3+}.

TABLE II. Asymptotic separated-atom energies of BH^{3+}.

Molecular state	Asymptotic atomic states	Energy (eV)		
		Theory	Experiment [15]	Difference
$1\,^2\Sigma^+$	$B^{2+}(2s)+H^+$	0	0	0
$2\,^2\Sigma^+$	$B^{2+}(2p\sigma)+H^+$	6.005	5.999	0.006
$1\,^2\Pi$	$B^{2+}(2p\pi)+H^+$	6.005	5.999	0.006
$3\,^2\Sigma^+$	B^{3+}+H(1s)	24.320	24.333	0.013
$4\,^2\Sigma^+$	$B^{2+}(3s)+H^+$	22.332	22.343	0.011
$5\,^2\Sigma^+$	$B^{2+}(3p\sigma)+H^+$	23.923	23.924	0.001
$2\,^2\Pi$	$B^{2+}(3p\pi)+H^+$	23.923	23.924	0.001
$6\,^2\Sigma^+$	$B^{2+}(3d\sigma)+H^+$	24.309	24.310	0.001
$3\,^2\Pi$	$B^{2+}(3d\pi)+H^+$	24.309	24.310	0.001

It can be seen from Fig. 5 that the molecular states $1\,^2\Sigma^+$, $2\,^2\Sigma^+$, and $1\,^2\Pi$, which asymptotically correlate with the $B^{2+}(n=2)+H^+$ charge-exchange channels, energetically lie below the initial $3\,^2\Sigma^+$state. The radiative decay of $3\,^2\Sigma^+$ to these three states is responsible for the radiative charge transfer in this collision system. Figure 8 shows the dipole transition moments between the $3\,^2\Sigma^+$ state and $1\,^2\Sigma^+$, $2\,^2\Sigma^+$, and $1\,^2\Pi$ states.

III. THEORETICAL METHODS

A. QMOCC method for nonradiative charge transfer

The QMOCC method, which is only briefly outlined here, has been described in detail elsewhere [22,23]. It involves solution of a coupled set of second-order differential equations using the log-derivative method of Johnson [24]. In the adiabatic representation, transitions between channels are driven by radial and rotational (A^r and A^θ) couplings of the vector potential $\vec{A}(\vec{R})$, where $\vec{R}$ is the internuclear distance vector. Since the adiabatic description contains first- and second-order derivatives, it is numerically convenient to make a unitary transformation [23,25] to a diabatic representation. With the diabatic potentials and couplings, the coupled set of second-order differential equations is solved and matched to the plane-wave boundary conditions at a large internuclear distance, $R_{\max}$, to obtain the K matrix. Then the differential cross section from channel α to channel β can be expressed in terms of the S-matrix elements

$$\frac{d\sigma_{\alpha\to\beta}}{d\Omega}=\frac{1}{4k_\alpha^2}\left|\sum_J(2J+1)\left(\delta_{\alpha\beta}-S^J_{\alpha\beta}\right)P_J(\cos\theta)\right|^2, \quad (2)$$

where k_α denotes the initial momentum of center-of-mass motion, J is total angular momentum quantum number, and P_J is the Legendre polynomial of order J. The integral cross section is obtained by integration over the full scattering solid angle Ω, which yields

$$\sigma_{\alpha\to\beta}=\frac{\pi}{k_\alpha^2}\sum_J(2J+1)\left|\delta_{\alpha\beta}-S^J_{\alpha\beta}\right|^2. \quad (3)$$

B. AOCC method for nonradiative charge transfer

The semiclassical TC-AOCC equations are obtained by expanding the total electron wave function Ψ in terms of bound atomic orbitals of the two ionic centers, (ϕ^A,ϕ^B), multiplied by plane wave ETFs,

$$\Psi(\vec{r},t)=\sum_i a_i(t)\phi_i^A(\vec{r},t)+\sum_j b_j(t)\phi_j^B(\vec{r},t), \quad (4)$$

and by inserting this expansion into the time-dependent Schrödinger equation [26]. In ion-atom collision systems, the straight-line approximation is normally adopted for the relative nuclear motion. In the present calculations, we employ the frozen core approximation for the Be^{2+} and B^{3+} ions.

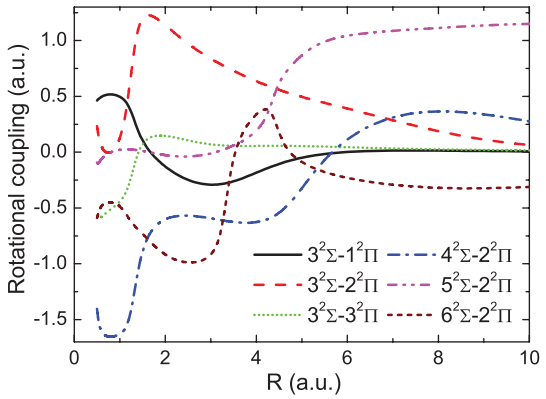

FIG. 7. (Color online) Rotational coupling matrix elements for BH^{3+}.

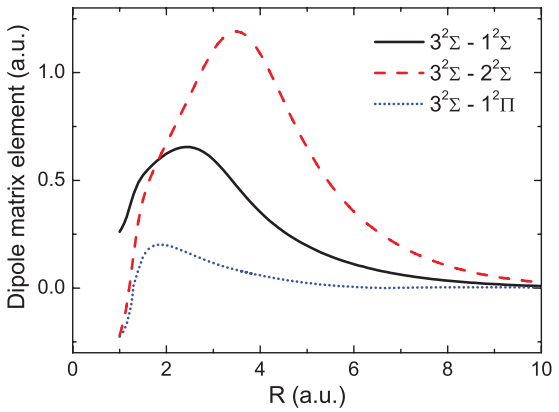

FIG. 8. (Color online) Dipole transition matrix elements for BH^{3+}.

The interaction of the active electron with the ionic cores can be expressed as [8] (for Be^{2+}) and as [7] (for B^{3+}):

$$V_{Be^{2+}}(r) = -\frac{2}{r} - \frac{2}{r}e^{-4.37792r} - 3.4616e^{-4.3792r}, \quad (5)$$

$$V_{Be^{3+}}(r) = -\frac{3}{r} - \frac{2}{r}e^{-6.0817r} - 6.0817e^{-6.0817r}. \quad (6)$$

The resulting first-order coupled equations for the amplitudes $a_i(t)$ and $b_j(t)$ are

$$\begin{aligned} i(\dot{A} + S\dot{B}) &= HA + KB, \\ i(\dot{B} + S^{\dagger}\dot{A}) &= \bar{K}A + \bar{H}B, \end{aligned} \quad (7)$$

where A and B are the vectors of the amplitudes a_i and b_j, respectively. S is the overlap matrix ($S^{\dagger}$ is its transposed form), H and $\bar{H}$ are direct coupling matrices, and K and $\bar{K}$ are the electron exchange matrices. The cross section for $1 \rightarrow j$ electron capture transitions are calculated as

$$\sigma_{cx,j} = 2\pi \int_0^{\infty} |b_j(+\infty)|^2 b db, \quad (8)$$

where b is the impact parameter.

The sum of $\sigma_{cx,j}$ over j gives the corresponding total electron capture cross section. The expansion basis used in the present TC-AOCC calculations includes all states centered on H having principal quantum number $n \leqslant 3$ and all states on the ionic centers Be^{2+} and B^{3+} having principal quantum number $n \leqslant 7$, without the $6h$,$7h$, and $7i$ orbitals. We note that in our previous study of Be^{2+},B^{3+} + H collision systems [9], the basis on the Be^{2+} and B^{3+} centers included only the states with $n \leqslant 6$. The expanded basis used in the present calculations affects the electron capture cross sections only for energies above 50 keV/u.

C. Optical potential and semiclassical methods for radiative charge transfer

In the optical potential method [27–29], the radiative decay cross section has the form

$$\sigma(E) = \frac{\pi}{k_A^2} \sum_J^{\infty} (2J+1)[1 - \exp(-4\eta_J)], \quad (9)$$

with the phase shift η_J calculated in the distorted-wave approximation:

$$\eta_J = \frac{\pi}{2} \int_0^{\infty} dR \left| f_J^A(k_A R) \right|^2 A(R), \quad (10)$$

where $A(R)$ is the probability for the radiative transition,

$$A(R) = \frac{4}{3} D^2(R) \frac{|V_A(R) - V_X(R)|^3}{c^3}. \quad (11)$$

$D(R)$ is the dipole transition moment, $V_A(R)$ and $V_X(R)$ are the potential energy curves of the upper and lower states involved in the transition, and c is the speed of light. The optical potential method gives an upper limit of the fully quantal radiative decay cross section [27–29]. Because all the final states of collision systems investigated here are repulsive states, the radiative decay contributes only to the charge-transfer process.

The optical potential method provides an adequate description of the radiative decay process only at low (below ~0.1 eV) collision energies. In order to extend our radiative decay calculations to higher energies, we replace the summation in Eq. (9) by an integration and use the JWKB approximation for the phase shifts. The semiclassical radiative decay cross section is then obtained in the form [27,30]

$$\sigma(E) = 2\pi \sqrt{\frac{2\mu}{E}} \int b db \int_{R_A^{CTP}}^{\infty} dR \frac{A(R)}{\sqrt{1 - [V_A(R)/E] - (b^2/R^2)}}, \quad (12)$$

where b is the impact parameter and R_A^{CTP} is the classical turning point in the incoming channel.

IV. RADIATIVE AND NONRADIATIVE CHARGE TRANSFER IN $Be^{2+}(1s^2)$ + H(1s) COLLISIONS

A. $Be^{2+}(1s^2)$ + H(1s) → Be^{+} + H^{+}

The nonradiative charge-transfer cross sections for $Be^{2+}(1s^2)$ + H(1s) collisions are calculated by the QMOCC method and AOCC method in the energy range 10^{-8}–10 keV/u and 0.1–100 keV/u, respectively. In the QMOCC calculation, the values of R_{max} for matching the boundary conditions are taken from 10 000 a.u. to 500 a.u. for the collision energy that varies from 10^{-8} to 10 keV/u, respectively. Beyond $R = 30$ a.u., the potential of the $2\,^2\Sigma^+$ state was extended to larger internuclear distances by the dipole polarization potential $V_{pol}(R) = -\alpha_d q^2/2R^4$, where $\alpha_d = 4.5$ a.u. is the dipole polarizability of the H(1s) atom and $q = 2$ is the charge of the Be^{2+} ion. The long-range asymptotic behavior of other states is described by the Coulomb form. Two-channel and nine-channel calculations were performed in the energy ranges 10^{-8}–10^{-2} keV/u and 10^{-2}–10 keV/u, respectively, and the results matched smoothly at 10^{-2} keV/u. The total nonradiative charge-transfer cross sections calculated by the QMOCC and AOCC methods are displayed in Fig. 9 in the energy range of 10^{-3}–100 keV/u and are compared with the results of the perturbed stationary states (PSS) method

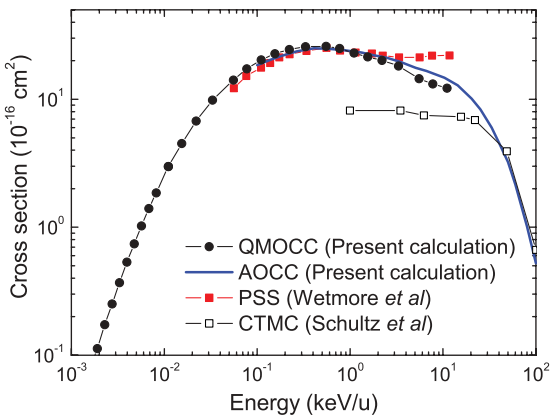

FIG. 9. (Color online) The total nonradiative charge-transfer cross sections for the $Be^{2+}(1s^2)$ + H(1s) collision. Present QMOCC calculation (solid line with filled circles); present AOCC results (solid line); PSS results of Wetmore *et al.* [4] (solid line with filled squares); CTMC results of Schultz *et al.* [3] (solid line with open squares).

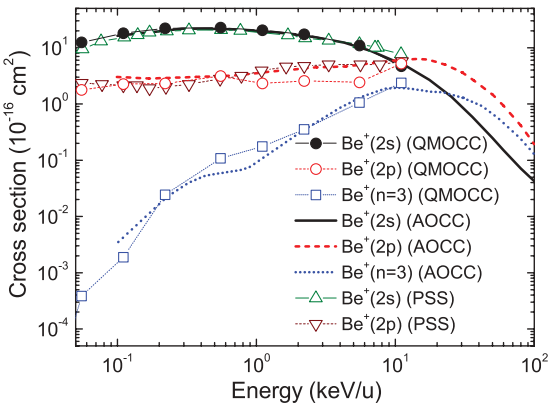

FIG. 10. (Color online) State-selective cross sections of present QMOCC and AOCC results and the PSS results of Ref. [4] for electron capture to the $2s$, $2p$, and $n = 3$ states of Be^+ ions.

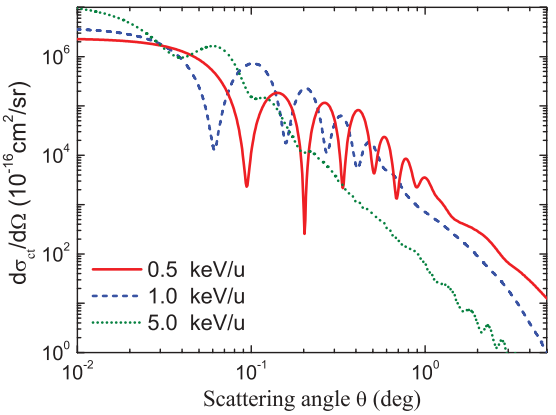

FIG. 11. (Color online) Differential cross sections for nonradiative charge transfer of $Be^{2+}(1s^2) + H(1s)$ collision.

obtained by Wetmore *et al.* [4] and with the classical trajectory Monte Carlo (CTMC) results of Schultz *et al.* [3]. Our QMOCC and AOCC results are in good mutual agreement in the overlapping energy range as well as with the PSS results of Wetmore *et al.* [4]. The CTMC results agree well with our AOCC results for energies above 50 keV/u but lie significantly below ours for energies smaller than 20 keV/u. (The application of the CTMC method below 25 keV/u is known to be inappropriate [19].) In the energy range 3–10 keV/u, the QMOCC results are somewhat lower than the AOCC results. This may be because of the difficulties (and related to them, slightly reduced accuracy) in the calculation of potential energy curves and coupling matrix elements in the small R region, which is important for high-energy collision dynamics.

The state-selective cross sections for electron capture to $Be^+(2s)$, $Be^+(2p)$, and $Be^+(n = 3)$ states obtained by the QMOCC and AOCC methods are shown in Fig. 10 and compared with the PSS results [4]. Our QMOCC results are coincident with the AOCC results and the PSS results [4] on the whole, especially for energies below 1 keV/u. The capture to the $Be^+(2s)$ state is dominant in the energy region E < 10 keV/u because of the strong coupling of $1\,^2\Sigma$ and $2\,^2\Sigma$ states mentioned earlier. Since this coupling appears at relatively large internuclear distances (about 6.7 a.u.), the charge-transfer cross section reaches its maximum at relatively low collision energies (about 0.5 keV/u). The charge transfer to the $Be^+(2p)$ state becomes important at energies above several keV/u (and dominant for energies above 10 keV/u) because of the radial coupling between $2\,^2\Sigma$ and $3\,^2\Sigma$ states, contributing to the population of the $Be^+(2p_0)$ state, and the rotational $2\,^2\Sigma$–$1\,^2\Pi$ coupling, contributing to the population of $Be^+(2p_1)$ states, which acquire their maximum values at internuclear distances about 3 a.u. and 2 a.u., respectively (see Figs. 2 and 3), that can be reached at high collision energies only. We should mention that the states $1\,^2\Sigma$ and $3\,^2\Sigma$, populated by their radial coupling with the initial $2\,^2\Sigma$ state during the incoming stage of the collision, both have strong rotational coupling with the $1\,^2\Pi$ state, which contributes to the population of the $Be^+(2p_1)$ asymptotic state.

The $Be^+(n = 3) + H^+$ channels are weak charge-transfer channels at low collision energies as they are all connected with the small populations of the $3\,^2\Sigma$ state during the incoming stage of the collision by the weak $2\,^2\Sigma$–$3\,^2\Sigma$ coupling at $R \approx 3$ a.u. At $R \approx 2$ a.u., the $3\,^2\Sigma$ is strongly radially coupled with the $4\,^2\Sigma$ state (see Fig. 2), which asymptotically correlates with the $Be^+(3s) + H^+$ channel. During the receding stage of the collision, the $4\,^2\Sigma$ state becomes strongly coupled with the $5\,^2\Sigma$ state (at $R \approx 5.5$ a.u.; see Fig. 2) that asymptotically correlates with the $Be^+(3p_0) + H^+$ channel. The $3\,^2\Sigma$ state at small internuclear distances is rotationally coupled to the $2\,^2\Pi$ state, which correlates with the $Be^+(3p_1) + H^+$ charge-transfer channel. As the small internuclear distances where all these couplings are located can be reached at higher collision energies only, the cross sections for $Be^+(3l) + H^+$ charge-transfer channels become comparable to those of the $Be^+(2l) + H^+$ only at energies about 10 keV/u and above (see Fig. 10).

To provide additional information about the charge-exchange dynamics, the differential charge-transfer cross sections have been calculated quantum mechanically by using Eq. (2). In Fig. 11, we show the differential cross section for the $Be^{2+} + H(1s)$ collision system for collision energies of 0.5, 1, and 5 keV/u. It can be observed that with increasing collision energy, the forward scattering becomes increasingly more pronounced, while the large-angle scattering differential cross section decreases. The interference structures in the angular range 0.05°–1° also decrease with increasing energy.

B. $Be^{2+}(1s^2) + H(1s) \rightarrow Be^+(2s) + H^+ + h\nu$

The radiative decay of the initial $2\,^2\Sigma^+$ state of the $Be^{2+} + H(1s)$ collision system is possible only to the lower $1\,^2\Sigma^+$ state of this system, representing the $Be^+(2s) + H^+$ charge-exchange channel. Using the optical-potential method, we have calculated the radiative charge-transfer (RCT) cross section for energies from 10^{-5} to 0.1 eV/u, and the result is shown in Fig. 12. For comparison, the nonradiative charge-transfer (NRCT) cross section calculated by the QMOCC method is also shown in the figure. It should be noted that the nonradiative charge-transfer cross section starts to increase with decreasing energy below ~0.04 eV/u, a consequence of the increased role of the long-range polarization interaction in the collision system. The NRCT cross section in this

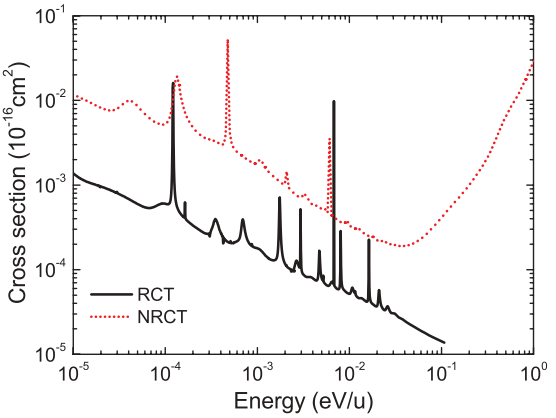

FIG. 12. (Color online) Comparison of radiative charge-transfer (RCT) and nonradiative charge-transfer (NRCT) cross sections for $Be^{2+}(1s^2) + H(1s)$ collisions.

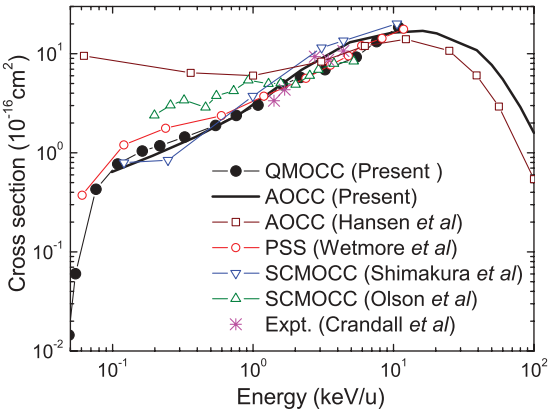

FIG. 13. (Color online) Total nonradiative charge-transfer cross sections for $B^{3+}(1s^2) + H(1s)$ collisions. Shown are present QMOCC results (solid line with filled circles); present AOCC results (solid line); AOCC results of Hansen *et al.* [7] (solid line with open squares); PSS results of Wetmore *et al.* [4] (solid line with open circles); SC-MOCC results of Shimakura *et al.* [6] (solid line with downward triangle); SC-MOCC results of Olson *et al.* [5] (solid line with upward triangle); and experiment results of Crandall *et al.* [10] (stars).

energy region is roughly an order of magnitude larger than the cross section for RCT. Both RCT and NRCT cross sections exhibit rich resonance structures in the energy region below ~0.03 eV. These resonances are attributed to the presence of quasibound rotational-vibrational states in the entrance channel. Because in the calculation of radiative charge transfer by optical-potential method the adiabatic effects are ignored, the positions of the peaks in the RCT and NRCT cross sections do not always coincide.

V. RADIATIVE AND NONRADIATIVE CHARGE TRANSFER IN $B^{3+}(1s^2) + H(1s)$ COLLISIONS

A. $B^{3+}(1s^2) + H(1s) \rightarrow B^{2+} + H^+$

We have performed cross section calculations for the nonradiative charge transfer in the $B^{3+}(1s^2) + H(1s)$ collision system using the QMOCC method in the energy range 10^{-8}–10 keV/u and the AOCC method in the energy range 0.1–100 keV/u. The total nonradiative charge-transfer cross sections in the energy range of 0.05–100 keV/u are shown in Fig. 13 and compared with the experimental results of Crandall *et al.* [10], the PSS results of Wetmore *et al.* [4], the semiclassical MOCC (SC-MOCC) results of Olson *et al.* [5] and Shimakura *et al.* [6], and the AOCC results of Hansen and Dubois [7]. In the overlapping energy range of 0.1–10 keV, our QMOCC results are in good agreement with our own AOCC results, with the experimental data [10], and with most other theoretical results. In the energy region below 2 keV/u, the AOCC results by Hansen and Dubois [7] are significantly larger than the results of present calculations as well as those of other authors, most probably because of some numerical error in the integration.

The maximum of the total cross section appears at a relatively large energy of about 15 keV/u because, as we have seen in Sec. II B, the strong coupling between the initial and final states appears at small internuclear distances. The sharp decrease of the charge-transfer cross section below ~0.1 keV/u is an indication of the absence of strong couplings at large internuclear distances in this collision system, as discussed in Sec. II B.

The cross sections for capture to $n = 2$ and $n = 3$ shells of the B^{2+} ion are shown in Fig. 14, together with the AOCC results of Hansen and Dubois [7]. The present QMOCC and AOCC results for $n = 3$ are in good mutual agreement in the overlapping energy range, while those for $n = 2$ disagree both below 1 keV/u and above 5 keV/u. The origin of this disagreement is the use of model potential (6), which, for the low-lying $n = 2$ states, apparently does not describe adequately the electron interaction with the ion core. The capture to $n = 3$ shells dominates up to $E = 1$–2 keV/u, when the capture to $n = 2$ also becomes significant.

The differential charge-transfer cross sections for the $B^{3+}(1s^2) + H(1s)$ collision system are presented in Fig. 15 for collision energies of 0.5, 1, and 5 keV/u. Compared to the $Be^{2+}(1s^2) + H(1s)$ case, the large-angle scattering becomes more pronounced in the present collision system because the potentials of the exit channels in BH^{3+} are more repulsive than those of the BeH^{2+} ion.

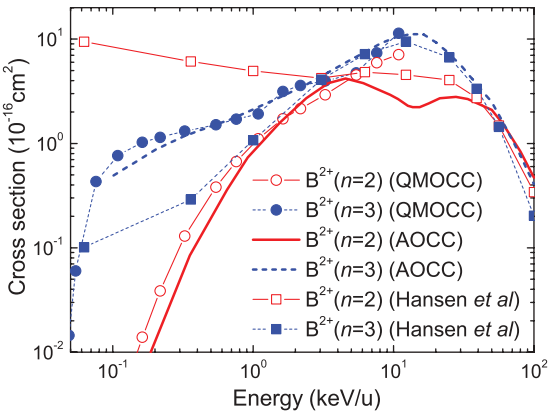

FIG. 14. (Color online) State-selective cross sections of present QMOCC and AOCC results and the AOCC results of Ref. [7] for electron capture to the $n = 2$ and $n = 3$ states of B^{2+} ions.

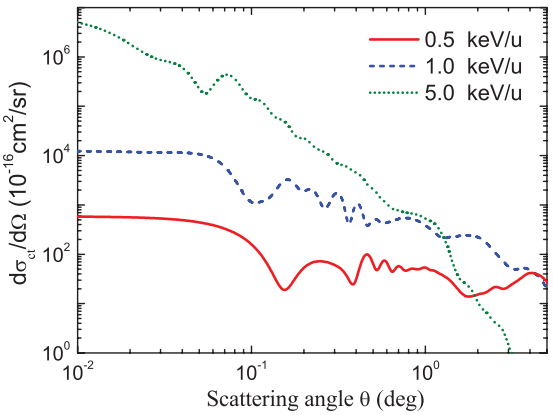

FIG. 15. (Color online) Differential cross sections for nonradiative charge transfer in $B^{3+}(1s^2) + H(1s)$ collisions.

B. $B^{3+}(1s^2) + H(1s) \rightarrow B^{2+}(n = 2) + H^+ + h\nu$

Using the optical potential and semiclassical methods, we have calculated the radiative charge-transfer cross sections to the three $B^{2+}(n = 2) + H^+$ channels ($1^2\Sigma^+$, $2^2\Sigma^+$, and $1^2\Pi$) in the energy range 10^{-5}–10 eV/u and 0.1–100 eV/u, respectively, as shown in Fig. 16. It can be seen that the results of the two methods join smoothly in the overlapping energy range. It should be noted, however, that the semiclassical method, by its nature, is unable to describe the resonances in the radiative decay cross sections since they have a pure quantum-mechanical origin.

The $2^2\Sigma^+$ state [corresponding to the $B^{2+}(2p\sigma) + H^+$ asymptotic state] is the most important radiative decay channel because of its large dipole moment with the initial channel (see Fig. 8). The $1^2\Sigma^+$ state [corresponding to the $B^{2+}(2s) + H^+$ asymptotic state] becomes most important for E > 30 eV/u because the dipole moment between $1^2\Sigma^+$ and $3^2\Sigma^+$ becomes large at small internuclear distances. We note that the radiative decay to the $1^2\Pi$ state [correlating to the $B^{2+}(2p\pi) + H^+$ asymptotic state] is more than two orders of magnitude weaker than for the other two states, reflecting its weak radiative coupling with the $3^2\Sigma^+$ states (see Fig. 8).

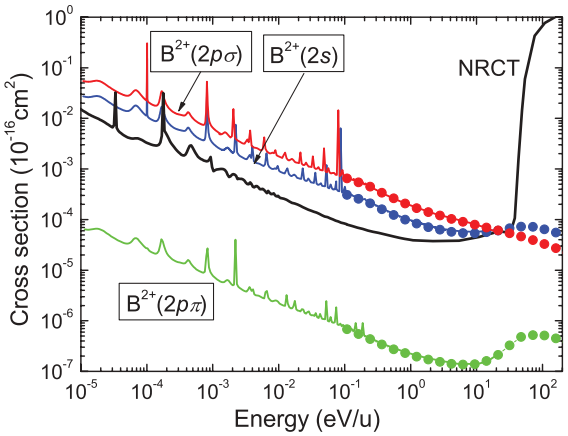

FIG. 16. (Color online) Radiative and nonradiative charge-transfer cross sections for $B^{3+}(1s^2) + H(1s)$ collisions. The radiative charge-transfer results are shown by the optical potential method (solid lines) and the semiclassical method (filled circles). Nonradiative charge-transfer results are shown by the solid line.

The nonradiative charge-transfer cross section calculated by the QMOCC method is also shown in the figure for comparison. For energies below 30 eV, the nonradiative charge-transfer cross section first decreases slowly, reaching a minimum at about 1 eV/u, and then starts to increase with decreasing energy. It should be noted that in the energy region below 10–20 eV/u, the cross sections of radiative charge-transfer channels $B^{2+}(2p\sigma) + H^+$ and $B^{2+}(2s) + H^+$ become significantly larger (up to a factor of 8 and 5 on average, respectively, below ~1eV/u) than the total nonradiative electron capture cross section. This is in contrast to the $Be^{2+} + H$ collision system, where nonradiative electron capture cross section was an order of magnitude larger than the radiative one in the energy region below 0.1 eV/u (cf. Fig. 12).

The drastic differences between the radiative and nonradiative cross sections in Figs. 12 and 16 can be easily understood on the basis of a semiclassical description of these processes. The nonradiative charge-transfer cross section in the region of its increase with decreasing the energy in these figures is determined essentially by the polarization interaction in the system for which the phase shifts and the summation in Eq. (3) can readily be calculated in the semiclassical approximation (see, e.g., [31]). As the polarization interactions in the $Be^{2+} + H$ and $B^{3+} + H$ systems differ only for the ratio 3/2, the nonradiative cross sections for the two systems in this energy region will be close to each other (see Figs. 12 and 16). On the other hand, the semiclassical radiative cross section [Eq. (12)] depends on the quantity $A(R)$, which, as seen from Eq. (11), is a strong function of the energy difference $|V_A(R) - V_X(R)|$ in the region where the dipole moment $D(R)$ takes its largest values and of the square of $D(R)$ itself. In the case of the $Be^{2+} + H$ system, the region of internuclear distances where $D(R)$ for the coupled states $2\,^2\Sigma$ and $1\,^2\Sigma$ acquires its largest values (around 6.7 a.u.; see Fig. 4) coincides with the region of avoided crossing of adiabatic potential energies of these two states, which is rather small (only 0.034 a.u. at $R = 6.7$ a.u.). In contrast to this, the energy differences $|V_A(R) - V_X(R)|$ between the $3\,^2\Sigma$–$2\,^2\Sigma$ and $3\,^2\Sigma$–$1\,^2\Sigma$ states in the $B^{3+} + H$ system have very large values (see Fig. 5) in the internuclear distance regions where their dipole moments attain large values (see Fig. 8). The large values of $|V_A(R) - V_X(R)|$ for these states compensate for their relative modest dipole moments (with respect to that for the $2\,^2\Sigma$–$1\,^2\Sigma$ transition in $Be^{2+} + H$) and bring the RCT cross section significantly above the nonradiative one. This analysis indicates that if the initial and final charge-transfer channels in an ion-atom system are coupled nonadiabatically (radially) and are strongly coupled at certain internuclear distance R_x, their radiative charge-transfer cross section will be small despite their strong radiative coupling in the region around R_x. For the radially weakly coupled initial and final charge-transfer channels, it appears, according to Eqs. (11) and (12), that the opposite is true, opening the possibility for the radiative channel to become the dominant charge-transfer channel.

VI. CONCLUSIONS

In this article, we have studied the radiative and nonradiative electron capture processes in the $Be^{2+}(1s^2) + H(1s)$ and $B^{3+}(1s^2) + H(1s)$ collision systems in a broad range of collision energies. The total and state-selective cross sections for the nonradiative electron capture have been calculated using the QMOCC method in the energy range 10^{-8}–10 keV/u and using the TC-AOCC method in the energy range 0.1–100 keV/u. The results of the two methods for the total and dominant channel capture cross sections agree very well in the overlapping energy range. They also agree with the available experimental data (for $B^{3+} + H$ [10]) and are in fair agreement with the results of other theoretical calculations employing the semiclassical MOCC and AOCC methods with smaller expansion bases. (An exception is the results of the AOCC calculations of Hansen and Dubois [7], in which an obvious numerical error is present.) For both collision systems, we have also calculated the differential charge-transfer cross sections for collision energies of 0.5, 1, and 5 keV/u.

The radiative charge-transfer cross sections have been calculated using the optical potential method in the energy range 10^{-5}–0.1 eV/u and the semiclassical method in the energy range 0.1–100 eV/u. The results of the two methods join each other smoothly at ∼0.1 eV/u. It has been found that in the case of the $Be^{2+}(1s^2) + H(1s)$ collision system, the nonradiative charge-transfer cross section is an order of magnitude larger than the radiative one for energies below 0.1 eV/u, whereas in the $B^{3+}(1s^2) + H(1s)$ collision case, the cross sections for radiative capture channels $B^{2+}(2p\sigma) + H^+$ and $B^{2+}(2s) + H^+$ are significantly larger than the total nonradiative electron capture cross section in the energy region below 10–20 eV/u. The significant differences in the magnitudes of the radiative charge-transfer cross sections in the two studied collision systems have been understood on the basis of energy differences between the radiatively coupled states in the regions of internuclear distances where corresponding dipole moments are dominantly distributed. The value of the dipole moment, although entering quadratically the (semiclassical) radiative charge-transfer cross section, has a relatively smaller effect on the magnitude of the RCT cross section. Both radiative and nonradiative charge-transfer cross sections increase with decreasing collision energy in the region below ∼0.1 eV/u for $Be^{2+}(1s^2) + H(1s)$ and ∼1 eV/u for $B^{3+}(1s^2) + H(1s)$, in accordance with general theories of these processes.

ACKNOWLEDGMENTS

This work was supported in part by the International Atomic Energy Agency (Vienna, Austria) under Research Contracts No. 15689/R0 with R.K.J. and No. 15700/R0 with J.G.W., the National Natural Science Foundation of China (Grants No. 10974021, No. 10875017, and No. 10979007), and the National Key Laboratory of Computational Physics Foundation under Grant No. 9140C6904030808.

[1] A. Loarte *et al.*, Nucl. Fusion **47**, S203 (2007).
[2] D. R. Bates and B. L. Moiseiwitsch, Proc. Phys. Soc. **67**, 805 (1954); D. R. Bates, H. C. Johnston, and I. Stewart, *ibid.* **84**, 517 (1964).
[3] D. R. Schultz, P. S. Krstić, and C. O. Reinhold, Phys. Scr. T **62**, 69 (1996).
[4] A. E. Wetmore, H. R. Cole, and R. E. Olson, J. Phys. B **19**, 1515 (1986).
[5] R. E. Olson, E. J. Shipsey, and J. C. Browne, J. Phys. B **11**, 699 (1978).
[6] N. Shimakura, S. Suzuki, Y. Murakami, J. P. Gu, G. Hirsch, R. J. Buenker, M. Kimura, and I. Shimamura, Phys. Scr. T **62**, 39 (1996).
[7] J. P. Hansen and A. Dubois, Phys. Scr. T **62**, 55 (1996).
[8] M. Das, M. Purkait, and C. R. Mandal, J. Phys. B **31**, 4387 (1998).
[9] L. Liu, D. Jakimovski, J. G. Wang, and R. K. Janev, J. Phys. B **43**, 144005 (2010).
[10] D. H. Crandall, R. A. Phaneuf, and F. W. Meyer, Phys. Rev. A **19**, 504 (1979).
[11] S. Lepp, P. C. Stancil, and A. Dalgarno, J. Phys. B **35**, R57 (2002).
[12] R. J. Buenker and R. A. Phillips, J. Mol. Struct. Theochem. **123**, 291 (1985).
[13] S. Krebs and R. J. Buenker, J. Chem. Phys. **103**, 5613 (1995).
[14] T. H. Dunning, Jr., J. Chem. Phys. **90**, 1007 (1989).
[15] Yu. Ralchenko, A. E. Kramida, J. Reader, and NIST ASD Team, NIST Atomic Spectra Database (version 3.1.5), [http://physics.nist.gov/asd3] (2008).
[16] B. Herrero, I. L. Cooper, and A. S. Dickinson, J. Phys. B **29**, 5583 (1996).
[17] G. Hirsch, P. J. Bruna, R. J. Buenker, and S. D. Peyerimhoff, Chem. Phys. **45**, 335 (1980).
[18] M. Gargaud, R. McCarroll, and P. Valiron, J. Phys. B **20**, 1555 (1987).
[19] B. H. Bransden and M. R. C. McDowell, *Charge Exchange and the Theory of Ion-Atom Collisions* (Clarendon, Oxford, 1992).
[20] M. C. Bacchus-Montabonel and P. Ceyzeriat, Phys. Rev. A **58**, 1162 (1998).
[21] L. F. Errea, L. Mendez, and A. Riera, J. Phys. B **15**, 101 (1982).
[22] M. Kimura and N. F. Lane, Adv. At. Mol. Opt. Phys. **26**, 79 (1990).
[23] B. Zygelman, D. L. Cooper, M. J. Ford, A. Dalgarno, J. Gerratt, and M. Raimondi, Phys. Rev. A **46**, 3846 (1992).
[24] B. R. Johnson, J. Comput. Phys. **13**, 445 (1973).
[25] T. G. Heil, S. E. Butler, and A. Dalgarno, Phys. Rev. A **23**, 1100 (1981).
[26] W. Fritsch and C. D. Lin, Phys. Rep. **202**, 1 (1991).
[27] B. Zygelman and A. Dalgarno, Phys. Rev. A **38**, 1877 (1988).
[28] P. C. Stancil and B. Zygelman, Astrophys. J. **472**, 102 (1996).
[29] L. B. Zhao, J. G. Wang, P. C. Stancil, J. P. Gu, H.-P. Liebermann, R. J. Buenker, and M. Kimura, J. Phys. B **39**, 5151 (2006).
[30] D. R. Bates, Mon. Not. R. Astron. Soc. **111**, 303 (1951).
[31] N. F. Mott and H. S. W. Massey, *The Theory of Atomic Collisions*, 3rd ed. (Oxford University Press, Oxford, 1965).